JOURNAL OF GEOPHYSICAL RESEARCH, VOL. 114, A10301, doi:10.1029/2009JA014213, 2009

Click Here for Full Article

Penetration of ELF currents and electromagnetic fields into the Earth's equatorial ionosphere

B. Eliasson[1,2] and K. Papadopoulos[3]

Received 4 March 2009; revised 16 June 2009; accepted 25 June 2009; published 3 October 2009.

[1] The penetration of extremely low frequency (ELF) transient electromagnetic fields and associated currents in the Earth's equatorial E-region plasma is studied theoretically and numerically. In the low-frequency regime, the plasma dynamics of the E-region is characterized by helicon waves since the ions are viscously coupled to neutrals while the electrons remain mobile. For typical equatorial E-region parameters, the plasma is magnetically insulated from penetration of very long timescale magnetic fields by a thin diffusive sheath. Wave penetration driven by a vertically incident pulse localized in space and time leads to both vertical penetration and the triggering of ELF helicon/whistler waves that carry currents obliquely to the magnetic field lines. The study presented here may have relevance for ELF wave generation by lightning discharges and seismic activity and can lead to new concepts in ELF/ULF injection in the earth-ionosphere waveguide.

Citation: Eliasson, B., and K. Papadopoulos (2009), Penetration of ELF currents and electromagnetic fields into the Earth's equatorial ionosphere, *J. Geophys. Res.*, *114*, A10301, doi:10.1029/2009JA014213.

1. Introduction

[2] The interaction of quasistatic electric fields with the equatorial E-region, the creation of the equatorial electrojet (EEJ) current and its observational consequences has been the subject of many experimental and theoretical studies [*Kelley and Heelis*, 1989; *Forbes*, 1981; *Rastogi*, 1989; *Onwumechili*, 1997; *Rishbeth*, 1997]. In this case, tidal motions drive and maintain horizontal (zonal) electric fields of the order .5–1 mV/m perpendicular to the ambient magnetic field over long times (several minutes to hours) and over a 600 km strip in the E-region (90–120 km) of the dip equatorial ionosphere. As discussed by previous authors, the small zonal electric field has significant consequences, because of the inhomogeneous conductivity structure of the E-region plasma. At steady state and to zero order, current continuity requires that a vertical polarization electric field be built to prevent the downward Hall current from flowing. This electric field is larger than the zonal electric field by the ratio of the Hall-to-Pedersen conductivity, approximately a factor 30, resulting in vertical electric fields in excess of 10 mV/m and associated with predominantly eastern electrojet currents of more than 10 A/km. As noted by *Forbes* [1981], current continuity requires the presence of a vertical current, with current closure established by field aligned currents. These currents result in ground based quasistationary magnetic fields of 100 nT or more.

[3] While the quasistationary EEJ electrodynamics has been well established, this is not the case for the field and current structures driven by relatively short time ($\sim 10^{-3}$–1 s), small scale size (50–100 km) horizontal electric fields associated with phenomena such as lightning discharges [*Helliwell et al.*, 1973; *Uman*, 1987; *Inan et al.*, 1985; *Berthelier et al.*, 2008; *Master and Uman*, 1983; *Milikh et al.*, 1995], impulsive fields created by seismic events [*Hayakawa et al.*, 2006] or generated by ground based horizontal electric dipole (HED) antennas [*Papadopoulos*, 2008]. It is the objective of the paper to study the physics of field penetration and current generation and redistribution associated with vertical incidence on the equatorial E-region of localized in space low frequency pulsed and continuous wavefields.

[4] The manuscript is organized as follows. The next section presents the plasma physics of the ionospheric layer including the boundary conditions between the ionosphere and free space where the magnetic field is obtained analytically. The numerical results are presented in section 3, and in section 4 wave penetration and energy injection mechanisms are discussed in more detail. Finally, in section 5 we briefly summarize of our results and discuss the limitations of the model and its future extensions.

2. Interaction Model

[5] Figure 1 shows typical profiles for the daytime conductivities of the equatorial ionosphere. The most important feature for the present work is the dominance of the Hall conductivity in the E-region 90–120 km. This is because in this range the electrons are strongly magnetized ($\nu_{en} \ll \omega_{ce}$) while the ions are unmagnetized and viscously coupled to the neutrals ($\nu_{in} \gg \omega_{ci}$). The plasma behavior in this range reminds us of the behavior of semiconductors and the dominant low frequency wave is the helicon mode

[1]Department of Physics, Umeå University, Umeå, Sweden.
[2]Theoretische Physik IV, Ruhr-Universität Bochum, Bochum, Germany.
[3]Departments of Physics and Astronomy, University of Maryland, College Park, Maryland, USA.

Copyright 2009 by the American Geophysical Union.
0148-0227/09/2009JA014213$09.00

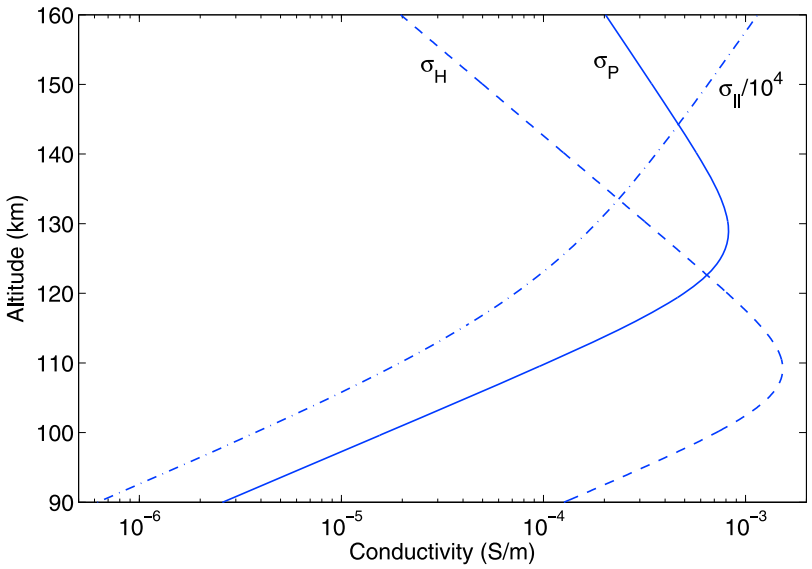

Figure 1. Numerical fits of the daytime vertical profiles of the parallel, Pedersen, and Hall conductivities $\sigma_\parallel$, σ_P, and σ_H, respectively [after *Forbes and Lindzen*, 1976], used in the numerical simulations with daytime conditions. The conductivities are decreased a factor 5 to simulate nighttime conditions.

[*Aigrain*, 1960]; namely whistler behavior extends to frequencies much lower than the ion cyclotron frequency.

[6] We assume a vertical incidence on the equatorial E-region of a magnetic impulse given by

$$\mathbf{B}_{ant}(x,y,z,t) = B_{ant}(t)\frac{\hat{\mathbf{x}}\bar{z} - \hat{\mathbf{z}}\bar{x}}{(\bar{x}^2+\bar{y}^2+\bar{z}^2)^{\alpha/2}}, \tag{1}$$

where $\mathbf{B}_{ant}(t)$ is the value of the antenna magnetic field at the bottom of the E-region taken at a height $z = z_0$, and the normalized coordinates are $\bar{x} = x/z_0$, $\bar{y} = y/z_0$, and $\bar{z} = z/z_0$. The value of α depends on the type of radiation structure or antenna. Since we are mainly interested in exploring the physics associated with the penetration and current structure of the E-region, we will assume a very simple model for the antenna, that of an equivalent infinite length wire in the y direction, located at $x = z = 0$, while we assume the ambient geomagnetic field in the x direction. The geometry of the model is illustrated in Figure 2. In this geometry we have $\alpha = 2$ and $\bar{y} = 0$ so that

$$\mathbf{B}_{ant}(x,z,t) = B_{ant}(t)\frac{\hat{\mathbf{x}}\bar{z} - \hat{\mathbf{z}}\bar{x}}{(\bar{x}^2+\bar{z}^2)}. \tag{2}$$

The result can easily be generalized to the case of a finite length antenna by taking $\alpha = 3$ [*Master and Uman*, 1983]. The ionospheric layer is treated as a two-dimensional layer varying in the geomagnetic field aligned direction x and the vertical direction z. The y direction is assumed to be homogeneous, consistently with equation (2). In this model, free space is below $z = 90$ km, while the ionospheric layer extends vertically above $z = 90$ km. The ionospheric layer and free space are magnetized by a constant external geomagnetic field $\mathbf{B}_0 = B_0\hat{\mathbf{x}}$, directed horizontally in the x direction.

[7] We discuss next the plasma model used for the ionospheric layer. The ionospheric electric field is related to the current density via the generalized Ohm's law

$$\begin{bmatrix} j_x \\ j_y \\ j_z \end{bmatrix} = \begin{bmatrix} \sigma_\parallel & 0 & 0 \\ 0 & \sigma_P & -\sigma_H \\ 0 & \sigma_H & \sigma_P \end{bmatrix} \begin{bmatrix} E_x \\ E_y \\ E_z \end{bmatrix}, \tag{3}$$

where $\sigma_\parallel$, σ_P and σ_H is the parallel, Pedersen, and Hall conductivity, respectively [*Kelley and Heelis*, 1989]. For a plasma with electrons and one ion species they are given by

$$\sigma_\parallel = \varepsilon_0\frac{\omega_{pe}^2}{\nu_{en}}, \tag{4}$$

$$\sigma_P = \varepsilon_0\frac{\omega_{pe}^2}{\omega_{ce}}\left[\frac{\nu_{en}\omega_{ce}}{\omega_{ce}^2+\nu_{en}^2} + \frac{\nu_{in}\omega_{ci}}{\omega_{ci}^2+\nu_{in}^2}\right], \tag{5}$$

and

$$\sigma_H = \varepsilon_0\frac{\omega_{pe}^2}{\omega_{ce}}\left[\frac{\omega_{ce}^2}{\omega_{ce}^2+\nu_{en}^2} - \frac{\omega_{ci}^2}{\omega_{ci}^2+\nu_{in}^2}\right]. \tag{6}$$

In the E-region, where $\omega_{ce} \gg \nu_{en}$ and $\omega_{ci} \ll \nu_{in}$ the Hall conductivity dominates and the plasma dynamics is dominated by helicon waves, while in the F-region where $\omega_{ce} \gg \nu_{en}$ and $\omega_{ci} \gg \nu_{in}$, the Hall conductivity quickly vanishes and we have a diffusive behavior of the plasma. In our numerical modeling, we have used numerical fits of

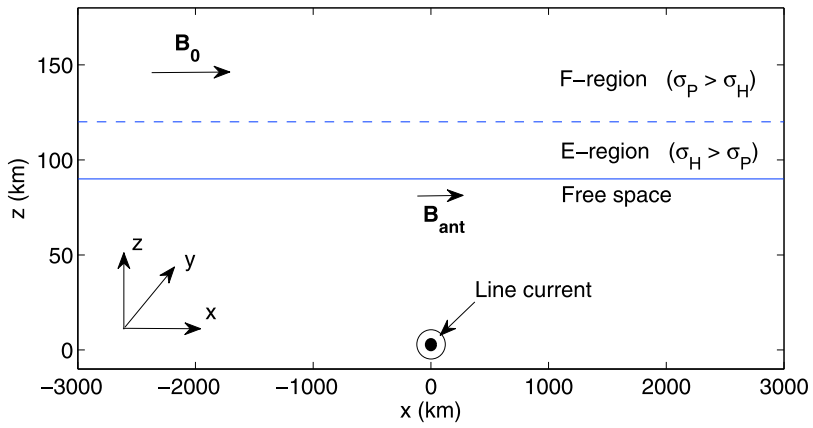

Figure 2. The geometry of the numerical model. The ionospheric layer is above $z = 90$ km, and free space is below $z = 90$ km. The constant geomagnetic field $\mathbf{B}_0$ is directed in the x direction. The impulse magnetic field $\mathbf{B}_{ant}$ at the bottom side ionosphere is created by an antenna placed at $x = z = 0$ and consisting of an infinitely long line current directed in the y direction. The simulation box starts at $x = -3000$ km and ends at $x = 3000$ km, and vertically it starts at $z = 90$ km and extends to $z = 160$ km. The E-region is characterized by $\sigma_H > \sigma_P$, while in the F-region, $\sigma_P > \sigma_H$.

typical vertical profiles of the conductivities in the equatorial E-region, by the functions

$$\sigma_{\parallel} = \frac{1}{a_{1,\parallel}\exp\left(-z/L_{1,\parallel}\right)n + a_{2,\parallel}\exp\left(-z/L_{2,\parallel}\right)}, \tag{7}$$

$$\sigma_P = \frac{1}{a_{1,P}\exp\left(-z/L_{1,P}\right) + a_{2,P}\exp\left(z/L_{2,P}\right)}, \tag{8}$$

and

$$\sigma_H = \frac{1}{a_{1,H}\exp\left(-z/L_{1,H}\right) + a_{2,H}\exp\left(z/L_{2,H}\right)}, \tag{9}$$

to approximate the parallel, Pedersen and Hall conductivities, respectively. We have chosen the sign in the second exponent of the denominator in formula (7) to be negative, since the parallel conductivity $\sigma_{\parallel}$ continues to increase at large altitudes. As a basis we used daytime profiles given by *Forbes and Lindzen* [1976]. In Table 1 we have listed parameter values used for day- and nighttime conditions, and have plotted the profiles for daytime conditions in Figure 1. For the nighttime conditions we simply assumed that the conductivities are decreased by a factor 5, accounting for the decreased electron and ion number densities. We note that the Hall conductivity dominates in the E-region below approximately 120 km while the Pedersen conductivity is dominant above 120 km. For the numerical treatment, it is convenient to invert the conductivity tensor to express the generalized Ohm's law by means of an impedance tensor,

$$\begin{bmatrix} E_x \\ E_y \\ E_z \end{bmatrix} = \begin{bmatrix} \rho_{\parallel} & 0 & 0 \\ 0 & \rho_P & \rho_H \\ 0 & -\rho_H & \rho_P \end{bmatrix} \begin{bmatrix} j_x \\ j_y \\ j_z \end{bmatrix}, \tag{10}$$

where the tensor components are $\rho_{\parallel} = 1/\sigma_{\parallel}$, $\rho_P = \sigma_P/(\sigma_P^2 + \sigma_H^2)$ and $\rho_H = \sigma_H/(\sigma_P^2 + \sigma_H^2)$. Combining equation (10) with Ampère's law

$$\nabla \times \mathbf{B} = \mu_0 \mathbf{j}, \tag{11}$$

and inserting the result into Faraday's law

$$\frac{\partial \mathbf{B}}{\partial t} = -\nabla \times \mathbf{E}, \tag{12}$$

we obtain the evolution equation

$$\frac{\partial \mathbf{B}}{\partial t} = -\frac{1}{\mu_0}\nabla \times \left[\overline{\overline{\rho}} \cdot (\nabla \times \mathbf{B})\right]. \tag{13}$$

Equation (13) governs Helicon waves in the E-layer where the impedance and conductivity tensors are nondiagonal,

Table 1. Parameter Values Used in the Numerical Fits (7)–(9) of the Conductivity Profiles (see Figure 1) in the Simulation Runs for Daytime and Nighttime Conditions

Parameter Values for Ionospheric Conductivities				
3*Daytime	$a_{1,\parallel} = 3.07 \times 10^9$ Ωm	$L_{1,\parallel} = 5.36$ km	$a_{2,\parallel} = 0.63 \times 10^3$ Ωm	$L_{2,\parallel} = 18$ km
	$a_{1,P} = 7.67 \times 10^{12}$ Ωm	$L_{1,P} = 5.36$ km	$a_{2,P} = 0.99$ Ωm	$L_{2,P} = 18.8$ km
	$a_{1,H} = 1.53 \times 10^{11}$ Ωm	$L_{1,H} = 5.36$ km	$a_{2,H} = 0.0157$ Ωm	$L_{2,H} = 10.67$ km
3*Nighttime	$a_{1,\parallel} = 1.535 \times 10^{10}$ Ωm	$L_{1,\parallel} = 5.36$ km	$a_{2,\parallel} = 3.15 \times 10^3$ Ωm	$L_{2,\parallel} = 18$ km
	$a_{1,P} = 3.835 \times 10^{13}$ Ωm	$L_{1,P} = 5.36$ km	$a_{2,P} = 4.95$ Ωm	$L_{2,P} = 18.8$ km
	$a_{1,H} = 7.65 \times 10^{11}$ Ωm	$L_{1,H} = 5.36$ km	$a_{2,H} = 0.0785$ Ωm	$L_{2,H} = 10.67$ km

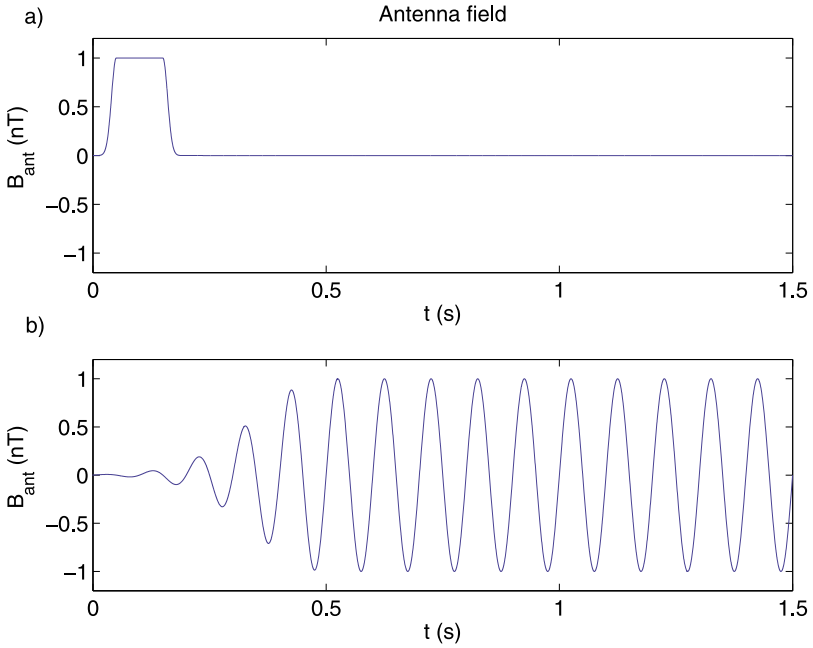

Figure 3. The time dependence of the antenna magnetic field used in the simulation runs: (a) pulsed antenna field and (b) continuous wave antenna field with frequency 10 Hz. The total simulation run is 1.5 s.

while it becomes diffusive-like in the F-layer where the impedance and conductivity tensors are diagonal.

[8] For simplicity we assume that the ionospheric plasma is vertically stratified so that $\rho_{\parallel}$, ρ_P and ρ_H depend only on the coordinate z. Writing out the components of equation (13), we then have

$$\frac{\partial B_x}{\partial t} = \frac{1}{\mu_0}\frac{\partial}{\partial z}\left[\rho_P\left(\frac{\partial B_x}{\partial z} - \frac{\partial B_z}{\partial x}\right) + \rho_H \frac{\partial B_y}{\partial x}\right], \tag{14}$$

$$\frac{\partial B_y}{\partial t} = -\frac{1}{\mu_0}\left[-\frac{\partial}{\partial z}\left(\rho_{\parallel}\frac{\partial B_y}{\partial z}\right) + \rho_H\left(\frac{\partial^2 B_x}{\partial x \partial z} - \frac{\partial^2 B_z}{\partial x^2}\right) - \rho_P \frac{\partial^2 B_y}{\partial x^2}\right] \tag{15}$$

and

$$\frac{\partial B_z}{\partial t} = -\frac{1}{\mu_0}\left[\rho_P\left(\frac{\partial^2 B_x}{\partial x \partial z} - \frac{\partial^2 B_z}{\partial x^2}\right) + \rho_H \frac{\partial^2 B_y}{\partial x^2}\right]. \tag{16}$$

Using the divergence condition for the magnetic field,

$$\frac{\partial B_x}{\partial x} = -\frac{\partial B_z}{\partial z}, \tag{17}$$

the B_x component can be eliminated from equations (15) and (16), so that we have two coupled equations

$$\frac{\partial B_y}{\partial t} = \frac{1}{\mu_0}\left[\frac{\partial}{\partial z}\left(\rho_{\parallel}\frac{\partial B_y}{\partial z}\right) + \rho_H\left(\frac{\partial^2 B_z}{\partial z^2} + \frac{\partial^2 B_z}{\partial x^2}\right) + \rho_P \frac{\partial^2 B_y}{\partial x^2}\right] \tag{18}$$

and

$$\frac{\partial B_z}{\partial t} = \frac{1}{\mu_0}\left[\rho_P\left(\frac{\partial^2 B_z}{\partial z^2} + \frac{\partial^2 B_z}{\partial x^2}\right) - \rho_H \frac{\partial^2 B_y}{\partial x^2}\right], \tag{19}$$

respectively, and equation (14) is a stand-alone equation. The x component of the magnetic field is readily obtained by equation (17).

[9] As boundary conditions at $z = z_0$ we will use that the normal magnetic field B_z and its z derivative, and the parallel (to the boundary surface in the $x - y$ plane) electric field components E_x and E_y, are continuous over the boundary, and we will use the free-space response of the magnetic field, which is evanescent for magnetic fields created by the plasma. A detailed discussion of the boundary conditions is given in Appendix A, while we only give the results here. The boundary conditions are most easily applied by first Fourier decomposing the solution in the x direction into a sum of terms proportional to $\exp(ik_x x)$ where k_x is the spatial wave number in the x direction. Then, for each wave number, the boundary condition are

$$\frac{\partial B_z}{\partial z} - |k_x| B_z = \frac{\partial B_{z,ant}}{\partial z} - |k_x| B_{z,ant}. \tag{20}$$

for B_z, while we set $B_y = 0$ at the boundary. The free space magnetic field is given by

$$\mathbf{B}_{free} = (\mathbf{B} - \mathbf{B}_{ant})_{z=z_0} \exp[|k_x|(z - z_0)] + \mathbf{B}_{ant}, \tag{21}$$

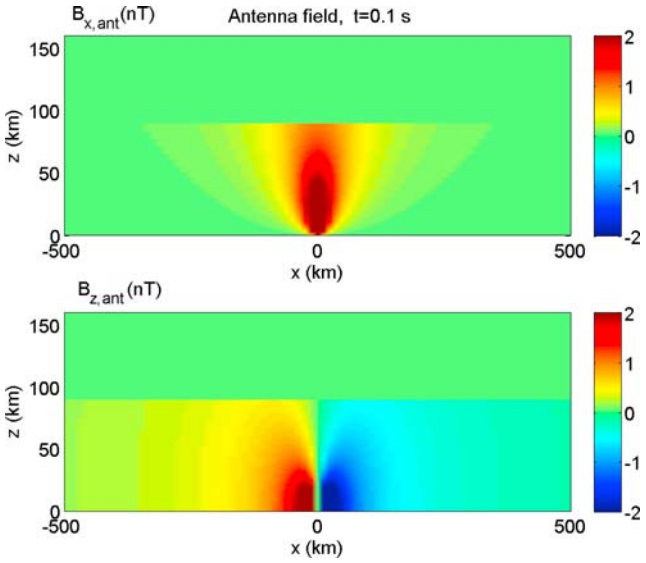

Figure 4. The pulsed free space antenna magnetic field x and z components $B_{x,ant}$ (top) and $B_{z,ant}$ (bottom) at time t = 0.1 s, when the antenna field has its maximum 1 nT at the plasma-free space boundary $z = z_0 = 90$ km. The y component of the antenna magnetic field is zero.

which is the sum of the magnetic field created by the ionosphere and that created by the antenna. The derivation of the free space magnetic field is given in Appendix A, where it is noted that it follows from Ampère's law that the y component of the free space magnetic field is zero.

[10] Equations (18)–(19), together with the boundary condition (20) for B_z and the appropriate choice of boundary condition for B_y, form a closed system.

3. Modeling Results

[11] We have conducted a series of numerical studies of the system (18)–(19) with parameters of interest to the equatorial E- and F-layers. Details of the numerical method are given in Appendix B. We have numerically studied one case with an unmodulated pulse and one case with a continuous wave antenna field. The time dependence of the antenna field for the two cases are shown in Figure 3. For the unmodulated pulse we use an antenna field of the form $B_{ant} = B_{0,ant} \exp[-(t - t_0)/2D_t^2]$ for $t < t_0$, $B_{ant} = B_{0,ant}$ for $t_0 \le t < t_1$ and $B_{ant} = B_{0,ant} \exp[-(t - t_1)/2D_t^2]$ for $t \ge t_1$, where the maximum amplitude $B_{0,ant}$ = 1 nT is reached at time t_0 = 0.05 s, and the pulse switched off smoothly at t_1 = 0.15 s, using the pulse rise and decay time D_t = 0.01 s. In Figure 4, the profile of the pulsed free space antenna magnetic field components $B_{x,ant}$ and $B_{z,ant}$ are shown at time t = 0.1 s, when the antenna field has its maximum 1 nT at the plasma-free space boundary $z = z_0$ = 90 km. For the continuous wave case we choose a 10 Hz antenna field that is ramped up smoothly so that $B_{ant} = B_{0,ant} \exp[-(t - t_0)/2\ D_t^2]\sin(20\pi\ t)$ for $t < t_0$ and $B_{ant} = B_{0,ant} \sin(20\pi\ t)$ for $t \ge t_0$, where the pulse reaches its maximum amplitude $B_{0,ant}$ = 1 nT at t_0 = 0.5 s, and the risetime is D_t = 0.15 s.

[12] Figures 5 and 6 show the spatial profiles of the magnetic field, current density and electric field for the

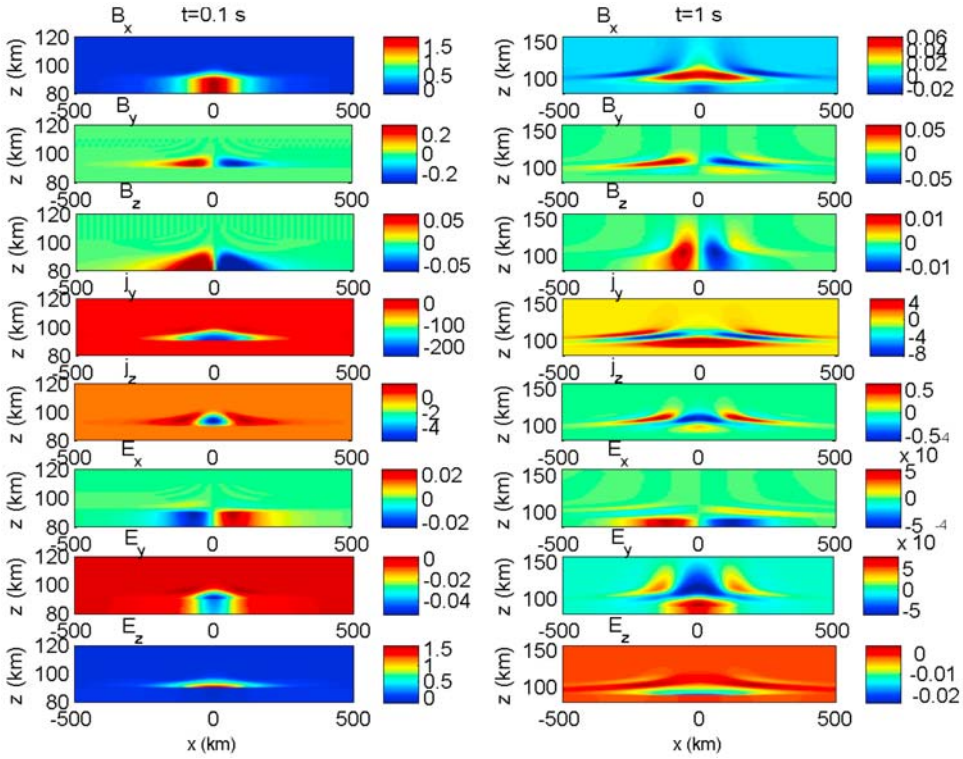

Figure 5. Simulation results at time (left) 0.1 s and (right) 1 s for daytime conditions for the pulsed antenna field (see Figure 3), showing the magnetic field components B_x, B_y, and B_z (nT), the current density components j_y and j_z (nA/m^2), and the electric field components E_x, E_y, and E_z (mV/m) (top to bottom). The total free space fields $\mathbf{B}_{free}$ and $\mathbf{E}_{free}$ are shown below z = 90 km.

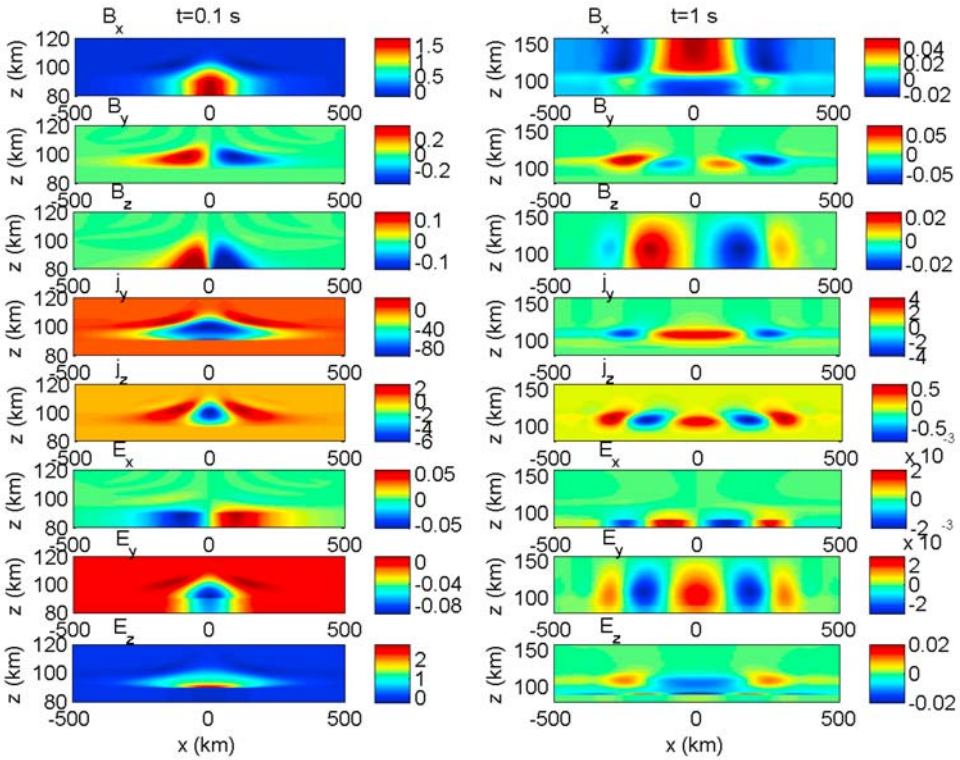

Figure 6. Simulation results at time (left) 0.1 s and (right) 1 s for nighttime conditions with a pulsed antenna field (see Figure 3), showing the magnetic field components B_x, B_y, and B_z (nT), current components j_y and j_z (nA/m^2), and electric field components E_x, E_y, and E_z (mV/m) (top to bottom). The total free space fields $\mathbf{B}_{free}$ and $\mathbf{E}_{free}$ are shown below z = 90 km.

unmodulated pulse case with daytime and nighttime ionospheric conductivity profiles, respectively, at time t = 0.1 s, when the imposed antenna field has its maximum, and in the relaxation phase after the pulse at time t = 1 s. The reconstruction of the electric field in the ionosphere and free space is discussed in Appendix A, while the horizontal and vertical current densities relate to the magnetic field via Ampère's law as

$$j_y = \frac{1}{\mu_0}\left(\frac{\partial B_x}{\partial z} - \frac{\partial B_z}{\partial x}\right), \tag{22}$$

and

$$j_z = \frac{1}{\mu_0}\frac{\partial B_y}{\partial x}, \tag{23}$$

respectively. (In free space the electric current is zero.) The first thing to notice at time t = 0.1 s is that at the ionospheric boundary at z = 90 km and x = 0, the horizontal magnetic field component B_x has a maximum value of ≈2 nT, twice the value of the imposed field in Figure 4, while the z component of the magnetic field (bottom row) is lower than the antenna field in Figure 4. The doubling of the horizontal field is easily explained by the fact that in order to shield the plasma interior from the incident magnetic field, the induced current layer should create inside the plasma a secondary field equal to and oppositely directed to the primary magnetic field. This induced current, directed in the y direction, will also create at the plasma-free space boundary a secondary magnetic field equal to and in the same direction as the incident field, thereby doubling the total field. The z component of the antenna field is partially canceled by the induced current. In examining Figure 5 we note that the interaction has the following dominant characteristics at t = 0.1 s:

[13] 1. The value of $E_z \approx 1.5$ mV/m is two orders of magnitude larger than the antenna driven E_y and appears to dominate the interaction.

[14] 2. The Hall current is apparently the cause of the large value of $j_y \approx -250$ nA/m^2.

[15] 3. The penetration distance is between 5 and 10 km. While this is of the order 50–60 times larger than the electron skin depth it is much less than the several hundred km's expected in a collisional unmagnetized plasma.

[16] Referring to equation (3) we note that

$$j_y = \sigma_P E_y - \sigma_H E_z, \tag{24}$$

and

$$j_z = \sigma_H E_y + \sigma_P E_z. \tag{25}$$

We see in Figure 5 that the large value of j_y is almost exclusively due to the Hall term, and by t = 0.05 s, it has propagated laterally almost 300 km in either side along with the associated B_y. This is a clear behavior of a current carrying helicon generated by the large E_z in the center of

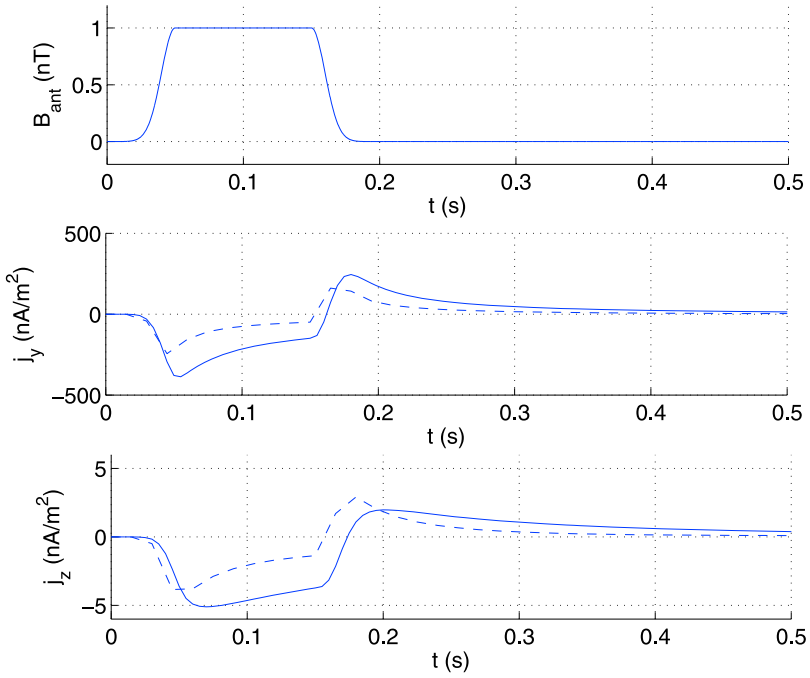

Figure 7. The time evolution of the (top) pulsed antenna field and (middle) horizontal and (bottom) vertical current densities j_y and j_z at z = 92 km, x = 0 for daytime (solid lines) and nighttime (dashed lines) conditions.

the pulse acting as an antenna. A key question is what limits the value of E_z? We recall that the equatorial electrojet [*Forbes*, 1981; *Kelley and Heelis*, 1989; *Rishbeth*, 1997] is due to a situation where tidal motion leads to a zonal electric field E_y. Due to current continuity, the vertical current j_z is prevented to flow and a large amplitude vertical electric field $E_z \approx -(\sigma_H/\sigma_P)E_y$ is built up, which leads to the intense zonal current $j_y = \sigma_C E_y$ where $\sigma_C = (\sigma_H^2/\sigma_P^2 + 1)\sigma_P$ is the Cowling conductivity. Signatures of this situation also appear in Figure 5 where E_z and j_y are large amplitude in a thin sheath near the boundary at z = 90 km. This thin sheath will be discussed further in section 4. However, here the presence of $E_y \approx 0.05$ mV/m also drives a vertical Hall current in the negative z direction of approximately 6 nA/m^2. The vertical current has also expanded horizontally with a downward current in the center flanked by upward currents at distances of ~100 km. Quasineutrality requires that a vertical electric field is built up to limit the vertical current to a value required by current continuity. This $\nabla \cdot \mathbf{j} = 0$ condition is controlled by the current density that can be carried by the helicons generated by E_z acting as a helicon antenna. Referring to Figure 5, we note that the horizontal current driven by the induced E_z = 1.5 mV/m is approximately 250 nA/m^2 in the negative y direction, while in Figure 6 we have E_z = 3 mV/m and the horizontal current 80 nA/m^2 in the negative y direction. The key role of helicon physics in the penetration and current spatiotemporal evolution is clearly seen at time t = 1 s in Figure 5, during the relaxation phase of the interaction. The magnetic pulse has driven helicons that are propagating at an angle between 15 and 20 degrees. The magnetic field has penetrated by approximately 30 km, indicating a penetration speed of ~30 km/s. Note that the wave speed is inversely proportional to the Hall conductivity and has a minimum at z = 110 km where the Hall conductivity has a maximum (see Figure 1). Near the boundary, the fields and currents have reversed sign and are decaying.

[17] The most striking difference between the run for daytime conditions in Figure 5 and nighttime conditions in Figure 6 is the enhanced wave penetration in the latter case. At time t = 0.1 s in Figure 6, we see a penetration of the B_y component of the magnetic field and by the associated current density j_z about 20 km into the plasma layer. At the later time t = 1 s, we see in Figure 6, that the magnetic field has fully penetrated the E-region layer and has reached the diffusive F-layer above 120 km. There are helicons with a typical wavelength of ~250 km propagating laterally in both directions, concentrated at the Hall conductivity maximum at z = 110 km, which seems to guide the helicon waves. The exact physics of the interaction at higher altitudes, where both the Hall and Pedersen conductivities vanish and the Alfvén wave dynamics becomes important, is under investigation and will be presented elsewhere; in our simulation study we have simply set the magnetic field components B_y and B_z to zero at the top boundary z = 160 km. The increase in wave penetration for nighttime conditions can be attributed to the increase of the wave speed of the helicons, which are inversely proportional to the Hall conductivity for a given length scale. In our case the typical length scale is the distance (= 90 km) between the antenna and the ionospheric layer, and for given times the penetration is a few times larger than in Figure 5.

[18] The time dependence of the y and z components of the current density at x = 0, z = 92 km is plotted in Figure 7. It shows that the current density follows the shape of the antenna field with a maximum value of $j_y = -400$ nA/m^2 for the daytime conditions and $j_y = -200$ nA/m^2 for nighttime conditions. The much weaker vertical current has a maxi-

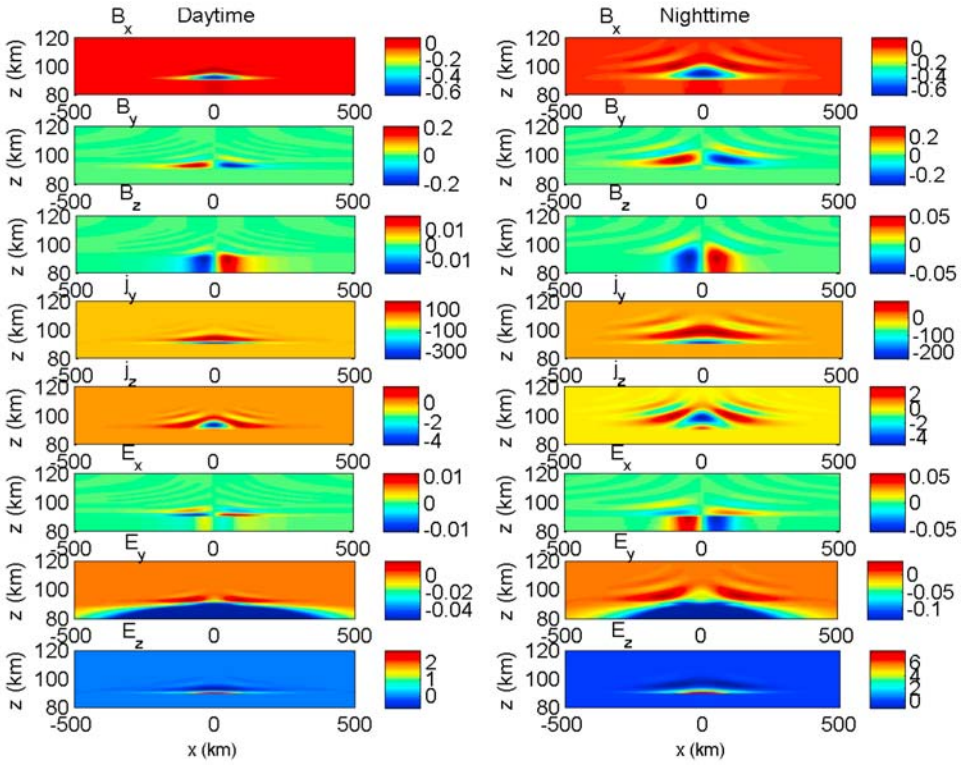

Figure 8. Simulation results at time 1.5 s for (left) daytime and (right) nighttime conditions for a continuous wave antenna field (see Figure 3), showing the magnetic field components B_x, B_y, and B_z (nT), current components j_y and j_z (nA/m^2), and electric field components E_x, E_y, and E_z (mV/m) (top to bottom). The total free space fields $\mathbf{B}_{free}$ and $\mathbf{E}_{free}$ are shown below z = 90 km.

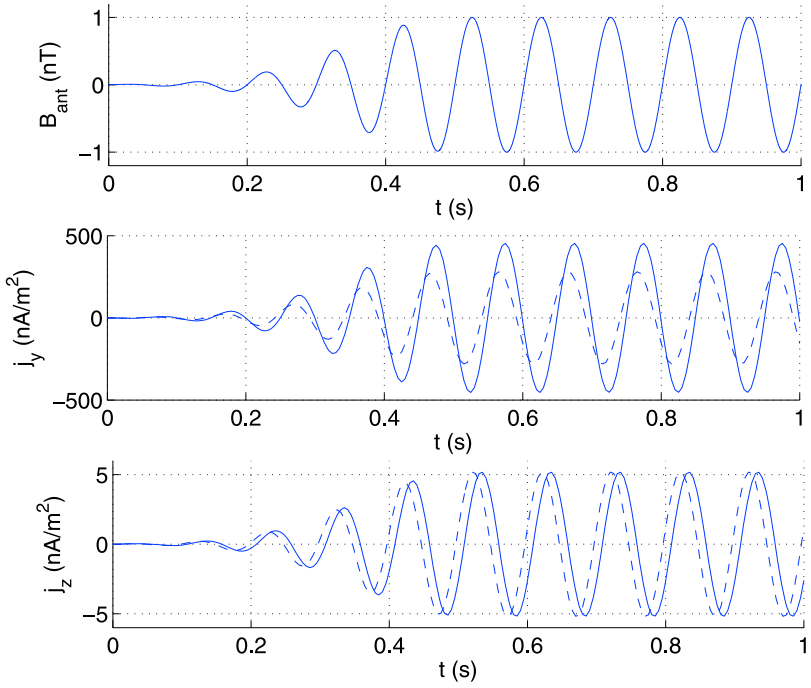

Figure 9. The time evolution of the (top) 10-Hz continuous wave antenna field and (middle) horizontal and (bottom) vertical current densities j_y and j_z at z = 92 km, x = 0 for daytime (solid lines) and nighttime (dashed lines) conditions.

mum value of $j_y = -5$ nA/m^2 for the daytime conditions and $j_y = -3$ nA/m^2 for nighttime conditions. There are clear overshoots of the current densities at the rise and fall of the antenna field at $t = 0.05$ s and $t = 0.15$ s.

[19] In Figures 8 and 9, we have displayed the numerical results from simulations where we instead used the continuous wave antenna field shown in Figure 3. The spatial profiles of the electromagnetic fields and currents are shown in Figure 8 for both daytime and nighttime at time $t = 1.5$ s, when the system has reached a steady oscillating state. We observe for this case that the generated waves are essentially confined in the E-layer below 120 km and only for nighttime conditions some wave energy reaches 120 km. Here the most dominant characteristics are, firstly, a narrow band of a few km at the boundary $z = 90$ km where we have a large amplitude zonal current j_y of a few hundred nA/m^2, supported by a large amplitude vertical electric field E_z also confined to a narrow region closest to the boundary. Second, there is a vertical current density j_z closest to the boundary, associated with a zonal electric field E_y. Note that at the time $t = 1.5$ s the antenna magnetic field has a positive time derivative, which by Faraday's law induces an antenna electric field E_y. This antenna electric field can be seen below $z = 90$ km in Figure 8. Finally, we have oblique helicon wave generation and propagation away from the antenna region, visible in the magnetic field component B_y and in the current densities j_y and j_z.

[20] In Figure 9, we show the current density at $z = 92$ km and $x = 0$ for the continuous wave case. It shows that the currents early reach a steady state oscillating field with the phase close to that of the antenna field. The signal is somewhat delayed for the daytime compared to the nighttime case, probably due to the lower wave propagation speed for the daytime conditions. While the horizontal current density is two orders of magnitude larger than the vertical density j_z, the difference between day- and nighttime conditions is relatively small.

4. Wave Penetration and Energy Injection Considerations

[21] It is interesting to study further the mechanisms for penetration of waves into the ionospheric layer. While diffusive effects are important for the structure of the magnetic field closest to the free space boundary, helicon wave dynamics gives rise to radiation and penetration of wave energy into the interior of the ionosphere. These effects can be estimated in some simplified models. We for simplicity here assume wave solutions where B_y and B_z are proportional to $\exp(ik_x x)$, and that the conductivities are constants. We have seen from the numerical results that in general the vertical gradients are much larger than the horizontal gradients, $|\partial^2/\partial z^2| \gg k_x^2$. In this limit, equations (18) and (19) take the form

$$\left(\frac{\partial}{\partial t} - \frac{\rho_\parallel}{\mu_0}\frac{\partial^2}{\partial z^2}\right)B_y = \frac{\rho_H}{\mu_0}\frac{\partial^2 B_z}{\partial z^2} \tag{26}$$

and

$$\left(\frac{\partial}{\partial t} - \frac{\rho_P}{\mu_0}\frac{\partial^2}{\partial z^2}\right)B_z = \frac{\rho_H}{\mu_0}k_x^2 B_y \tag{27}$$

respectively. In the small-length scale limit $|\partial/\partial t| \ll (\rho_\parallel/\mu_0)|\partial^2/\partial z^2|$, we have from equation (26) that $B_y = -(\rho_H/\rho_\parallel)B_z$, which inserted into equation (27) gives

$$\frac{\partial^2 B_z}{\partial z^2} - k_x^2\frac{\rho_H^2}{\rho_\parallel \rho_P}B_z = 0, \tag{28}$$

with evanescent solutions of the form

$$B_z = B_{z0}\exp\left(ik_x x - \frac{\rho_H}{\sqrt{\rho_\parallel \rho_P}}|k_x|z\right), \tag{29}$$

where $\rho_H/\sqrt{\rho_\parallel \rho_P} \approx \sqrt{\sigma_\parallel/\sigma_P}$ for $\sigma_H \gg \sigma_P$. This gives rise to a diffusive sheath at the bottom boundary with a typical width of $D = (\sigma_P/\sigma_\parallel)^{1/2}/|k_x|$. For example, a half-wavelength of $\sim$100 km (the typical width of the antenna field at the bottom side ionosphere) would give $k_x \sim \pi/(100 \times 10^3) = 3.2 \times 10^{-5}$ m^{-1}. Using the conductivities at $z = 90$ km for daytime conditions (see Figure 1), $\sigma_\parallel = 5 \times 10^{-3}$ S/m, $\sigma_H = 1.5 \times 10^{-4}$ S/m and $\sigma_P = 3 \times 10^{-6}$ S/m, gives $\sqrt{\sigma_\parallel/\sigma_P} = 40$ and a sheath width $D \approx 1$ km. Hence for $\sigma_\parallel \gg \sigma_H \gg \sigma_P$, the plasma is magnetically insulated from diffusive penetration of very low frequency magnetic fields. The thin diffusive sheath is associated with the thin and large amplitude current density in the y direction, clearly seen in for example Figure 5. It is related to B_z through Ampère's law as

$$j_y = \frac{1}{\mu_0}\left(\frac{\partial B_x}{\partial z} - \frac{\partial B_z}{\partial x}\right) = -\frac{1}{\mu_0}\left(\sqrt{\frac{\sigma_\parallel}{\sigma_P}}|k_x|B_x + ik_x B_z\right)$$
$$\approx \frac{1}{\mu_0}\frac{\sigma_\parallel}{\sigma_P}ik_x B_z, \tag{30}$$

where in the last equality we used the divergence condition $\partial B_x/\partial x + \partial B_z/\partial z = 0$, or $ik_x B_x = (\sigma_\parallel/\sigma_P)^{1/2}|k_x|B_z$, and that $\sigma_\parallel \gg \sigma_P$. On the other hand, using $B_y = -(\rho_H/\rho_\parallel)B_z \approx -(\sigma_\parallel/-(\sigma_\parallel/\sigma_H)B_z$ and Ampère's law, we have

$$j_z = \frac{1}{\mu_0}\frac{\partial B_y}{\partial x} = -ik_x\frac{1}{\mu_0}\frac{\sigma_\parallel}{\sigma_H}B_z, \tag{31}$$

which is a factor σ_H/σ_P smaller than j_y in equation (30). As noted before, one can indeed see in Figure 5 that j_y is larger than j_z by two orders of magnitude closest to the boundary at $z = 90$ km. The large amplitude j_y is associated with a large amplitude vertical electric field $E_z \approx -j_y/\sigma_H$ by equation (24).

[22] For perturbations in the opposite, large-length scale limit $(\rho_\parallel/\mu_0)|\partial^2/\partial z^2|$, $(\rho_P/\mu_0)|\partial^2/\partial z^2| \ll |\partial/\partial t|$ (but still $|\partial^2/\partial z^2| \gg k_x^2$), equations (26) and (27) can be combined to a wave equation

$$\frac{\partial^2 B_y}{\partial t^2} - \frac{\rho_H^2}{\mu_0^2}k_x^2\frac{\partial^2 B_y}{\partial z^2} = 0 \tag{32}$$

where $\rho_H \approx 1/\sigma_H$. It predicts a penetration speed of $v_p = |k_x|/(\mu_0\sigma_H)$. It is inversely proportional to the Hall conductivity (and electron number density), and the factor $|k_x|$ indicates that the penetration speed depends on the parallel length scale of the source. These waves correspond

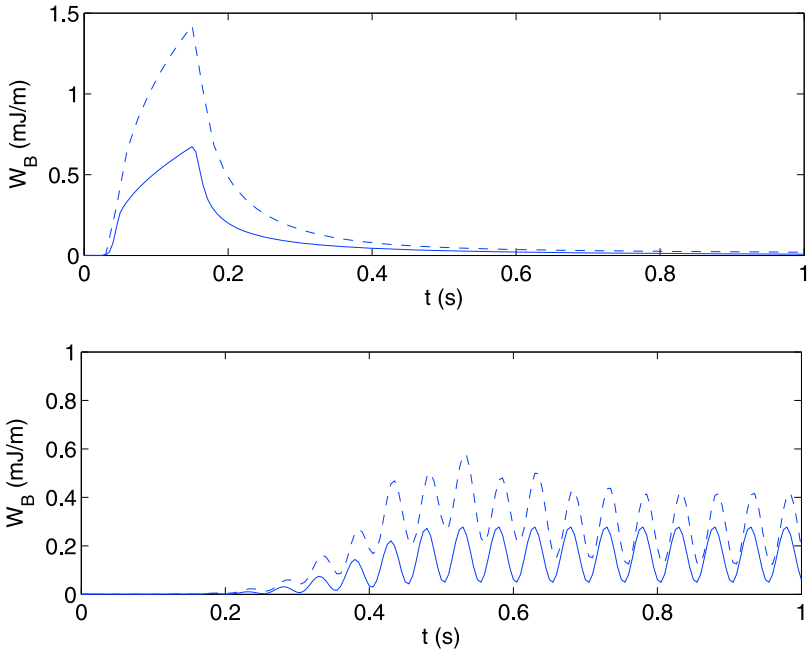

Figure 10. The integrated magnetic wave energy for (top) the pulsed antenna field and (bottom) the continuous wave antenna field for daytime (solid lines) and nighttime (dashed lines) conditions.

to obliquely propagating whistler/helicon waves. For example, a half-wavelength of ∼100 km would give $k_x \sim \pi/(100 \times 10^3) = 3.2 \times 10^{-5}$ m^{-1}, and using $\sigma_H = 1.5 \times 10^{-4}$ S/m, we would have a penetration speed of ∼170 km/s, while at $z = 110$ km where σ_H has its maximum, the penetration speed decreases one order of magnitude to ∼15 km. For the pulsed magnetic field case for daytime conditions in Figure 5 the waves have at $t = 0.1$ s penetrated about 30 km, corresponding to a mean wave speed of ∼30 km/s.

[23] Figure 10 shows the total magnetic wave energy in the ionosphere,

$$W_B = \iint \frac{B^2}{2\mu_0}\, dx\, dz \tag{33}$$

for the pulsed and continuous wave cases described above, where $B^2 = B_x^2 + B_y^2 + B_z^2$. The most efficient coupling of the wave energy to the ionosphere is for the nighttime conditions with lower conductivities (dashed line). The energy is in our geometry transferred from the antenna to the ionosphere via the z component of the Poynting flux $\mathbf{S} = \mathbf{E} \times \mathbf{B}/\mu_0$, i.e. via $S_z = -E_y B_x/\mu_0$. For the pulsed antenna field case in Figure 5 we see that that $E_y \approx -0.05$ mV/m and $B_x \approx 2$ nT at time $t = 0.1$ s in the region slightly below the plasma-free space boundary at $z = 90$ km. Integrating this field over the width of ∼100 km gives an energy flux of $\int S_z\, dx \sim 8 \times 10^{-3}$ Js^{-1}m^{-1}. In Figure 10 we see on the slope of the total energy as a function of time for the pulsed antenna field case for daytime conditions at time $t = 0.1$ s that the energy is increasing at a rate of $\sim 5 \times 10^{-3}$ Js^{-1}m^{-1}. This agrees fairly well with the prediction from the Poynting flux in free space below the ionosphere, taking into account that there are frictional losses in the ionosphere due to the Pedersen and parallel conductivities. For the nighttime conditions at the same time, the energy increase rate is approximately twice as large (see Figure 10), which is compatible with that the $E_y \approx -0.09$ mV/m at $t = 0.1$ s (see Figure 6), i.e. almost twice as large as for daytime conditions, while $B_x \approx 2$ nT is the same as for daytime conditions. We see for the pulsed antenna case in Figure 10 that there is a sharp increase of the energy at $t = 0.05$ s when the antenna pulse is switched on and a also a sharp drop of the energy when the antenna is switched off at $t = 0.15$ s. This may be attributed to the induced antenna electric field in the y direction which is proportional to the time derivative of the antenna current. The energy for the continuous wave case in Figure 10 reaches an oscillator quasisteady state at $t \sim 1$ s with a total energy approximately twice as large for the nighttime conditions compared to daytime conditions, due to the more efficient wave penetration for nighttime conditions discussed above.

5. Summary and Discussion

[24] We have studied theoretically and numerically the penetration of ELF electromagnetic fields and associated currents in the Earth's equatorial E-region plasma. The plasma is magnetically insulated from low frequency antenna magnetic field by a diffusive sheath whose vertical length scale is a factor $(\sigma_\parallel/\sigma_P)^{1/2}$ (1–2 orders of magnitude) smaller than the horizontal scale. Hence for an antenna field with a horizontal scale length of ∼100 km, we have a vertical diffusive penetration of a few kilometers or less for typical E-region parameters where the parallel conductivity $\sigma_\parallel$ is 2–4 orders of magnitude larger than the Pedersen conductivity σ_P. For transient and continuous wave antenna magnetic fields, there is also helicon/whistler wave penetration further into the plasma layer. The vertical wave penetration speed for typical daytime E-region parameters is of the order 10–200 km/s for a horizontal length scale of ∼100 km. The wave penetration speed is inversely

proportional to the Hall conductivity (and the electron number density); hence it has a minimum where the Hall conductivity has a maximum and is a few orders of magnitude larger for nighttime conditions than for daytime conditions. Wave penetration leads to both vertical penetration and the triggering of ELF helicon/whistler waves that carry information horizontally along the magnetic field lines, where the local maximum of the Hall conductivity profile can work as a waveguide for the helicon waves.

[25] Before closing we should remark on a potential application of the results in efficient generation and injection of ELF/ULF waves in the Earth-Ionosphere Waveguide (EIW). It is well known that Horizontal Electric Dipole (HED) antennas are extremely inefficient in injecting and propagating waves in the EIW (see for example, Special Issue of IEEE Transactions on Communications, Volume Com-22, No. 4, April 1974, p. 353–587). As discussed in detail by *Field et al.* [1989], at ELF frequencies and depending on the ground conductivity and frequency a Vertical Electric Dipole (VED) antenna radiates five more orders of magnitude than an HED having the same moment. In examining the results of our analysis of the interaction of the injected ELF pulse with the equatorial ionosphere, we note that the interaction resulted in the generation of both of boundary layer vertical as well as horizontal currents that will couple directly to the EIW modes. Furthermore, the excited helicon waves propagating along the local dipole magnetic field lines will renter the EIW at distances approximately 400 km in each side further exciting waveguide modes. The potential for developing an efficient ELF and ULF source for underground or underwater exploration or communications will be discussed in a future publication.

Appendix A: Boundary Conditions and Free Space Electromagnetic Fields

[26] We here derive the boundary conditions between the magnetic field $\mathbf{B}$ in the plasma and the magnetic field $\mathbf{B}_{\text{free}}$ in free space. The boundary conditions in the magnetostatic approximation are that the normal magnetic field component B_z and the parallel electric field components E_x and E_y should be continuous at the boundary. We will use that also the normal derivative $\partial B_z/\partial z$ is continuous at the boundary, as shown here. By noting that the electric field is always finite, we have from the generalized Ohm's law (equation (3)) that j_y and j_z are finite. (Only j_x may be infinite in the form of a surface current in the limit $\rho_{\|} = 0$.) Since j_y is finite, it follows from Ampère's law equation (11) that $\partial B_x/\partial z - \partial B_z/\partial x = \mu_0 j_y$ is finite and hence B_x is continuous at the boundary. This gives, from the divergence condition $\nabla \cdot \mathbf{B} = 0$, that $\partial B_z/\partial z = -\partial B_x/\partial x$ is continuous, and hence both B_z and $\partial B_z/\partial z$ are continuous at the boundary. It follows that also the parallel electric field components are continuous over the boundary: From Faraday's law we have that

$$\frac{\partial E_y}{\partial x} = -\frac{\partial B_z}{\partial t}, \tag{A1}$$

and since B_z is continuous it follows that E_y is continuous over the boundary. We also have that

$$\frac{\partial E_z}{\partial x} - \frac{\partial E_x}{\partial z} = \frac{\partial B_y}{\partial t}, \tag{A2}$$

and since both $\partial E_z/\partial x$ and $\partial B_y/\partial t$ are finite over the boundary, it follows that $\partial E_x/\partial z$ is finite over the boundary, and therefore E_x must be continuous over the boundary. Hence both the parallel components E_y and E_x and the normal magnetic field component B_z are continuous over the boundary, as required.

[27] To model the coupling of the antenna field to the ionosphere, we derive analytic solutions of the free-space magnetic field and couple it to the ionosphere via boundary conditions at the ionosphere-free space boundary at $z = z_0$. For this purpose is convenient to decompose the solutions into components proportional to $\exp(ik_x x)$ and consider one wave mode at the time, and to find the total solution as a sum or integral over k_x of the wave modes at the end. Since we have no free electrons in free space, the electric current is zero there, and hence we have $\nabla \times \mathbf{B}_{free} = 0$. Combining this with $\nabla \cdot \mathbf{B}_{\text{free}} = 0$, we have the vacuum response

$$\nabla^2 \mathbf{B}_{free} = 0. \tag{A3}$$

If we neglect current sources in the ground, then $\mathbf{B}_{\text{free}}$ is evanescent below the boundary at $z = z_0$, and we can analytically solve equation (A3) to find solutions on the form

$$\mathbf{B}_{free} = \hat{\mathbf{B}}_{free}(t) \exp[ik_x x + |k_x|(z - z_0)]. \tag{A4}$$

for a given wave number k_x. Using that the normal component B_z and its derivative $\partial B_z/\partial z$ is continuous over the boundary, i.e. $B_z = B_{z,free}$ and $\partial B_z/\partial z = \partial B_{z,free}/\partial z$, we have the boundary condition (for each k_x)

$$\frac{\partial B_{z,k_x}}{\partial z} = |k_x| B_{z,k_x}. \tag{A5}$$

For B_y, in the limit $\rho_{\|} = 0$, equation (18) is solved on the boundary $z = z_0$, while below the boundary, in free space, it follows from Ampère's law that $B_y = 0$. Hence in the limit $\rho_{\|} = 0$, there is a jump in B_y, associated with a horizontal line current along the boundary in the x direction. In the case $\rho_{\|} > 0$, we must specify a boundary condition for B_y, and we will for this case choose $B_y = 0$ at the boundary $z = z_0$ so that B_y connects smoothly to the vacuum value $B_y = 0$.

[28] Taking into account the antenna field (2), then we know (since we do not have plasma in free space) that the total magnetic field in free space is the external magnetic field generated by the antenna plus the one generated by the overhead plasma, $\mathbf{B}_{free} = \mathbf{B}_{ant} + \mathbf{B}_{pl}$. In free space below the plasma boundary, the field generated by the plasma is evanescent and has solutions on the form

$$\mathbf{B}_{pl} = \hat{\mathbf{B}}_{pl}(t) \exp[ik_x x + |k_x|(z - z_0)]. \tag{A6}$$

We again require that the z component of the magnetic field and its normal derivative are continuous at the boundary so that $B_z = B_{z,free}$ and $\partial B_z/\partial z = \partial B_{z,free}/\partial z$. Thus

$$B_z = B_{z,ant} + B_{z,pl} \tag{A7}$$

and

$$\frac{\partial B_z}{\partial z} = \frac{\partial B_{z,ant}}{\partial z} + \frac{\partial B_{z,pl}}{\partial z} = \frac{\partial B_{z,ant}}{\partial z} + |k_x| B_{z,pl} = \frac{\partial B_{z,ant}}{\partial z} + |k_x|\left(B_z - B_{z,ant}\right), \tag{A8}$$

or

$$\frac{\partial B_z}{\partial z} - |k_x| B_z = \frac{\partial B_{z,ant}}{\partial z} - |k_x| B_{z,ant}, \tag{A9}$$

which is the boundary condition given in equation (20). The boundary condition (A9) couples the antenna source magnetic field to the plasma magnetic field. For B_y, we again solve equation (18) also along the boundary $z = z_0$ in the limit $\rho_\parallel = 0$, while in the case $\rho_\parallel > 0$ we use $B_y = 0$ at $z = z_0$. Below the boundary $z = z_0$, we have $B_y = 0$.

[29] The total free space magnetic field is the sum of the magnetic field generated by the ionopheric plasma and that generated by the antenna, $\mathbf{B}_{free} = \mathbf{B}_{pl} + \mathbf{B}_{ant}$. It can be reconstructed in the following manner. We first note that it follows from Ampère's law that the y component of the magnetic field is zero in free space, while both B_z and B_x are continuous over the boundary, and therefore only we consider the x and z components of the magnetic field here. At the boundary $z = z_0$, both the antenna field $\mathbf{B}_{ant}$ and the magnetic field $\mathbf{B}$ inside the plasma are known, and using that $\mathbf{B} = \mathbf{B}_{free}$ at $z = z_0$, we have that $\mathbf{B}_{pl} = \mathbf{B} - \mathbf{B}_{ant}$ at $z = z_0$. Using that $\mathbf{B}_{pl}$ is evanescent, we thus know that the field generated by the overhead plasma has the form (for each k_x) $\mathbf{B}_{pl} = (\mathbf{B} - \mathbf{B}_{\mathrm{ant}})_{z=z_0} \exp[|k_x|(z - z_0)]$. The total magnetic field in free space is obtained by adding the antenna field to $\mathbf{B}_{pl}$, or (for each k_x)

$$\mathbf{B}_{free} = (\mathbf{B} - \mathbf{B}_{ant})_{z=z_0} \exp[|k_x|(z - z_0)] + \mathbf{B}_{ant}, \tag{A10}$$

which is the one given in equation (21). An inverse Fourier transform of $\mathbf{B}_{free}$ in k_x space gives its dependence of the spatial variable x.

[30] The electric field can be found from the magnetic field in the ionosphere and free space in the following manner. In the ionosphere, the electric fields is obtained from Ohm's law (equation (10)) and Ampère's law (equation (11)) as

$$\mathbf{E} = \overline{\overline{\rho}} \cdot (\nabla \times \mathbf{B})/\mu_0. \tag{A11}$$

Writing out the components, we have

$$E_x = -\frac{\rho_\parallel}{\mu_0} \frac{\partial B_y}{\partial z}, \tag{A12}$$

$$E_y = \frac{\rho_H}{\mu_0} \frac{\partial B_y}{\partial x} + \frac{\rho_P}{\mu_0}\left(\frac{\partial B_x}{\partial z} - \frac{\partial B_z}{\partial x}\right), \tag{A13}$$

and

$$E_z = -\frac{\rho_H}{\mu_0}\left(\frac{\partial B_x}{\partial z} - \frac{\partial B_z}{\partial x}\right) + \frac{\rho_P}{\mu_0} \frac{\partial B_y}{\partial x}. \tag{A14}$$

Both E_x and E_y are continuous over the boundary between the plasma and free space. In free space the electric field obeys $\nabla \cdot \mathbf{E} = 0$, and since $\nabla \times \mathbf{B} = 0$ in free space, we have from Faraday's law that $\nabla \times (\nabla \times \mathbf{E}) = 0$, hence $\nabla^2 \mathbf{E} = 0$ in free space. Following the same discussion of as for the magnetic field, the electric field generated by the plasma is evanescent in free space, and hence the x and y components of the total electric field in free space are given by (for each k_x)

$$\mathbf{E}_{free} = (\mathbf{E} - E_{ant}\hat{\mathbf{y}})_{z=z_0} \exp[|k_x|(z - z_0)] + E_{ant}\hat{\mathbf{y}}, \tag{A15}$$

where we have used that the antenna electric field only have components in the y direction, $\mathbf{E}_{ant} = E_{ant}\hat{\mathbf{y}}$. The antenna electric field is obtained from Faraday's law $\partial \mathbf{B}_{ant}/\partial t = -\nabla \times \mathbf{E}_{ant}$ where $\mathbf{B}_{\mathrm{ant}}$ is given by equation (2), or writing out the components,

$$-\frac{\partial E_{ant}}{\partial x} = -\alpha(t) \frac{\overline{x}}{\overline{x}^2 + \overline{z}^2} \tag{A16}$$

and

$$\frac{\partial E_{ant}}{\partial z} = \alpha(t) \frac{\overline{z}}{\overline{x}^2 + \overline{z}^2}, \tag{A17}$$

where we have denoted

$$\alpha(t) = -B_{0,ant} \frac{t - t_0}{D_t^2} \exp\left[-\frac{(t - t_0)^2}{2D_t^2}\right]. \tag{A18}$$

Integration of equations (A16) and (A17) gives

$$E_{ant} = -\frac{\alpha(t)}{2} \ln\left(\overline{x}^2 + \overline{z}^2\right), \tag{A19}$$

plus an additive, time-dependent integration constant which will not influence the total electric field. The component E_z is obtained from Faraday's law and using that $B_y = 0$ in free space,

$$\frac{\partial E_z}{\partial x} = \frac{\partial E_x}{\partial z}. \tag{A20}$$

In the limit $\rho_\parallel = 0$, we have equation (10) that E_x is zero in the ionosphere, and since E_x is continuous over the ionosphere-free space boundary, it follows that E_x in zero

also in free space. Therefore it follows from equation (A20) that also $E_z = 0$ in free space in this case.

Appendix B: Numerical Procedure

[31] The coupled system (equations (18)–(19)) together with equation (17) and the boundary conditions are solved with a pseudospectral method used to calculate derivatives of the horizontal x coordinate in Fourier space, and centered difference schemes are used to calculate derivatives in z direction. The discrete Fourier transform in x space and its inverse are performed numerically with the fast Fourier transform (FFT) and its inverse. The standard 4th order Runge-Kutta method is used to do the time stepping. In the simulations, we have used 500 grid points in the x direction and 140 grid points in the z direction. The time step used was 0.05 ms for the high electron number density cases and 0.005 ms for the low density case described below, to ensure numerical stability. In the horizontal direction the simulation box starts at $x = -3000$ km and ends at $x = +3000$ km; this ensures that the simulation box is large enough to minimize finite box effects. At the top boundary at $z = 160$ km, the magnetic field components B_y and B_z are set to zero. At the bottom boundary at $z = 90$ km between the ionosphere and free space, the boundary conditions are applied by first Fourier transforming the necessary components in x space, apply the boundary conditions, and then inverse Fourier transforming the boundary. In Fourier space, the boundary condition (20) is calculated implicitly with a one-sided difference approximation of the first derivative on the left-hand side, as

$$\frac{B_{z,2} - B_{z,1}}{\Delta z} - |k_z| B_{z,1} = \frac{\partial B_{z,ant}}{\partial z} - |k_x| B_{z,ant}, \qquad \text{(B1)}$$

where Δz is the grid size in z direction, and $B_{z,1}$ is the unknown boundary value of the magnetic field and $B_{z,2}$ is the known value of the magnetic field at the neighboring grid point. The derivative $\partial B_{z,ant}/\partial z$ is calculated exactly from the analytic expression for the antenna field (2), and is evaluated at $z = z_0$, and is Fourier transformed in x space. Solving equation (B1) for $B_{z,1}$, we have the magnetic field at the boundary as

$$B_{z,1} = \frac{1}{1 + \Delta z |k_x|} \left[B_{z,2} - \Delta z \left(\frac{\partial B_{z,ant}}{\partial z} - |k_x| B_{z,ant} \right) \right], \qquad \text{(B2)}$$

for a given k_x. The result is numerically inverse Fourier transformed in k_x space to obtain the dependence of $B_{z,1}$ on the spatial variable x.

[32] **Acknowledgments.** This work was partially supported by the Swedish Research Council (VR) and by ONR MURI N00014-07-1-0789. We thank Xi Shao and Gennady Milikh of University of Maryland and T. Wallace, C. L. Chang and I. Doxas of BAE Systems-AT for useful discussions. B. E. acknowledges the hospitality of University of Maryland, where this work was carried out.

[33] Amitava Bhattacharjee thanks James Sheerin and another reviewer for their assistance in evaluating this paper.

References

Aigrain, P. (1960), Les "hélicons" dans les semiconducteurs, in *Proceedings of the International Conference on Semiconductor Physics, Prague, 1960*, p. 224, Czechoslovak Academy of Science, Prague, 1961.

Berthelier, J.-J., M. Malingre, R. Pfaff, E. Seran, R. Pottelette, J. Jasperse, J.-P. Lebreton, and M. Parrot (2008), Lightning-induced plasma turbulence and ion heating in equatorial ionospheric depletions, *Nat. Geosci.*, *1*, 101–105.

Field, E. C., Jr., L. R. Kies, P. R. Bannister, R. F. Ingram, W. D. Hopkins, and M. A. Roberts (1989), An aerostat-supported ELF/VLF transmitter, *Radio Sci.*, *24*, 235–246.

Forbes, J. M. (1981), The equatorial electrojet, *Rev. Geophys.*, *19*, 469–504.

Forbes, J. M., and R. S. Lindzen (1976), Atmospheric solar tides and their electrodynamic effects: II. The equatorial electrojet, *J. Atmos. Terr. Phys.*, *38*(9–10), 911–920.

Hayakawa, M., S. Pulinets, M. Parrot, and O. A. Molchanov (2006), Recent progress in seismo electromagnetics and related phenomena, *Phys. Chem. Earth, Parts A/B/C*, *31*(4–9), 129–131.

Helliwell, R. A., J. P. Katsufrakis, and M. L. Trimpi (1973), Whistler-induced amplitude perturbations in VLF propagation, *J. Geophys. Res.*, *78*, 4679–4688.

Inan, U. S., D. L. Carpenter, R. A. Helliwell, and J. P. Katsufrakis (1985), Subionospheric VLF/LF phase perturbations produced by lightning-whistler induced particle precipitation, *J. Geophys. Res.*, *90*, 7457–7469.

Kelley, M. C., and R. A. Heelis (1989), *The Earth's Ionosphere. Plasma Physics and Electrodynamics*, Acad. Press, San Diego, Calif.

Master, M. J., and A. M. Uman (1983), Transient electric and magnetic fields associated with establishing a finite electrostatic dipole, *Am. J. Phys.*, *51*(2), 118–126.

Milikh, G. M., K. Papadopoulos, and C. L. Chang (1995), On the physics of high altitude lightning, *Geophys. Res. Lett.*, *22*(2), 85–88.

Onwumechili, C. A. (1997), *The Equatorial Electrojet*, Gordon and Breach, New York.

Papadopoulos, K. (2008), Pulsed Artificial Electrojet Generation, *AGU*, Fall Meet. Suppl., Abstract SA42A-01.

Rastogi, R. G. (1989), The equatorial electrojet, in *Geomagnetism*, vol. 3, edited by J. Jacobs, pp. 461–525, Elsevier, New York.

Rishbeth, H. (1997), The ionospheric E-layer and F-layer dynamos — a tutorial review, *J. Atmos. Sol. Terr. Phys.*, *59*(15), 1873–1880.

Uman, M. A. (1987), The lightning discharge, *Int. Geophys. Ser.*, vol. 39, edited by W. L. Donn, Acad. Press, New York.

B. Eliasson, Department of Physics, Umeå University, SE-901 87 Umeå, Sweden. (bengt@tp4.rub.de)

K. Papadopoulos, Departments of Physics and Astronomy, University of Maryland, College Park, MD 20742-2421, USA. (dpapadop@umd.edu)